JOURNAL OF SOLID STATE CHEMISTRY

Volume 179, Number 2, February 2006

CONTENTS

Regular Articles

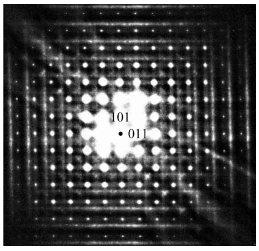

Shows typical $[1\bar{1}1]$ zone axis EDP for $Nb_3O_5F_5$. Note the strong essentially continuous, transverse polarized diffuse streaking along the $[h0l]^*$ and $[0kl]^*$ directions of reciprocal space. Such streaking is shown to be consistent with ordering of O/F along the **a** and **b** crystal directions.

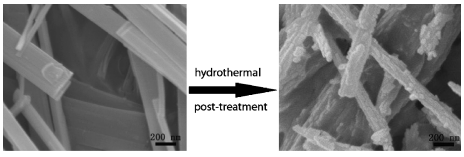

Hydrothermal post-treatment not only promoted the phase transformation from titanate to anatase TiO_2, but also was beneficial to the removal of Na^+ ions remained in the titanate nanoribbons.

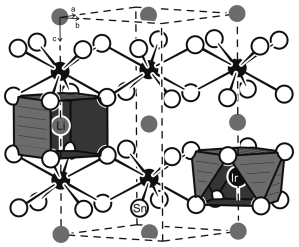

Crystal structure of tetragonal $LiIrSn_4$, space group $I4/mcm$. Lithium, iridium, and tin atoms are drawn as grey, filled, and open circles, respectively. The two-dimensional $[IrSn_4]$ network, the square-prismatic lithium and the square antiprismatic iridium coordination are emphasised.

Regular Articles—Continued

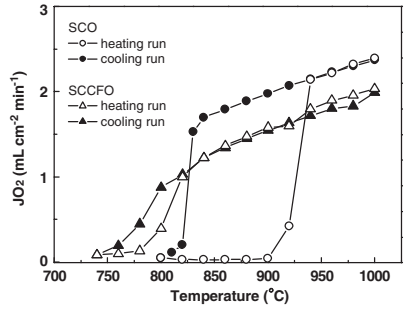

Temperature dependence of oxygen permeation rates through $Sr_{0.9}Ca_{0.1}Co_{0.89}Fe_{0.11}O_{3-\delta}$ (SCCFO) and $SrCoO_{3-\delta}$ (SCO) membranes with a thickness of 1.5 mm.

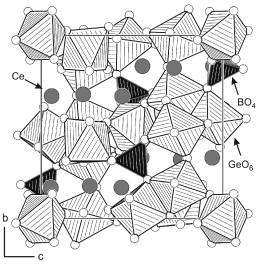

Synthesis of the new borogermanate $Ce_6(BO_4)_2Ge_9O_{22}$ via multianvil high-pressure techniques exhibiting BO_4-tetrahedra, GeO_6-octahedra, and oxygen atoms $O^{[3]}$ coordinated by one boron and two germanium atoms.

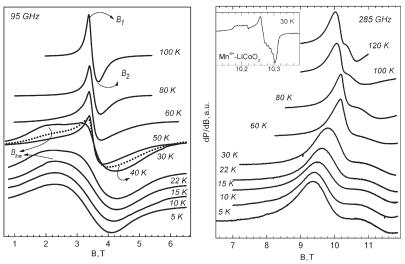

High-frequency EPR spectra of $LiNi_{0.5}Mn_{0.5}O_2$.

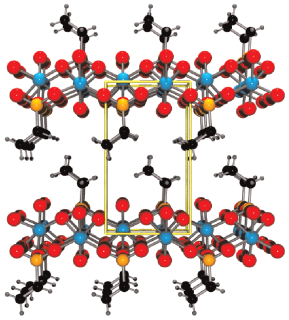

Ball and stick representation of the layered hybrid structure of $Co[(C_2H_5PO_3)(H_2O)]$.

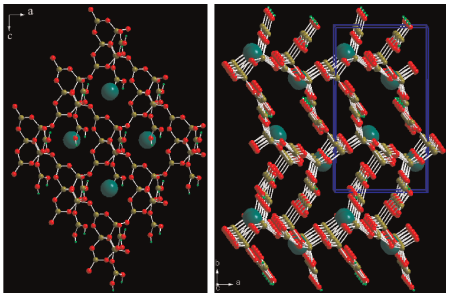

A new layered lead borate of $Pb[B_8O_{11}(OH)_4]$ has been synthesized under hydrothermal conditions. It consists of layers of 9-membered boron rings enclosing Pb^{2+} cations. Adjacent borate layers are interconnected via ionic Pb–O bonds and hydrogen bonding to form a 3D supramolecular network.

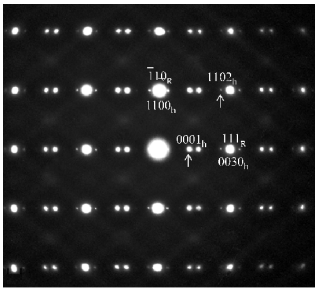

A $[11\bar{2}]_R \equiv [1\bar{1}0]_h$ zone axis EDP typical of incommensurately modulated "SnSb". Three integer indexation with the subscript "R" is with respect to the rhombohedral setting unit cell while the (3 + 1) integer (*hklm*) indexation with the subscript "h" is with respect to the hexagonal setting unit cell.

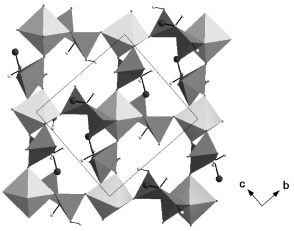

Based on aminomethylenediphosphonate, a zinc compound $Na_4Zn\{NH_3CH(PO_3)_2\}_2 \cdot 4H_2O$ (**1**) with 3D open-framework structure and two nickel compounds $Ni\{NH_3CH(PO_3H)_2\}_2 \cdot xH_2O$ (**2**) and $NaNi_2\{NH_3CH(PO_3)(PO_3H_{0.5})\}_2(H_2O)_2 \cdot 2H_2O$ (**3**) with square-grid layer and 3D open-framework structures, respectively, are reported. The magnetic studies of compounds **2** and **3** are also investigated.

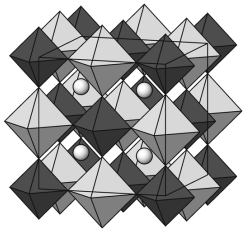

The monoclinic α-K_3AlF_6 phase is stable below 132 °C (a = 18.8588(2)Å, b = 34.0278(2)Å, c = 18.9231(1)Å, β = 90.453(1)°, SG $I2/a$ or Ia). The β phase exists in very narrow temperature interval between 132 and 153 °C. The orthorhombic γ polymorph is stable between 153 °C and 306 °C (a = 36.1229(6)Å, b = 17.1114(3)Å, c = 12.0502(3)Å, S.G. *Fddd*). Above 306 °C the cubic δ polymorph forms with a = 8.5786(4)Å and SG $Fm\bar{3}m$.

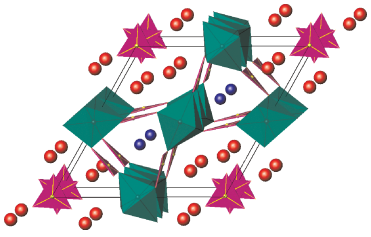

$YCa_3(MO)_3(BO_3)_4$ structure is constructed by MO_6 edge-shared chains interconnected by BO_3 groups with Y and Ca atoms occupying the triagonal and apatite-like tunnels.

Continued

Mechanochemical synthesis of rutile-type $CrMO_4$ (M = V, Sb) and their solid solutions
Takatoshi Tojo, Qiwu Zhang and Fumio Saito
Page 433

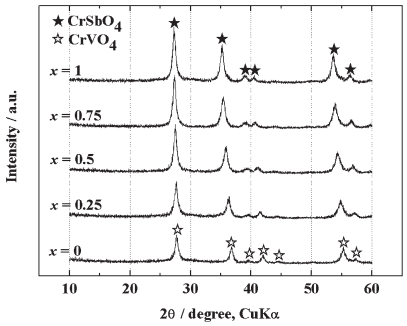

The solid solutions, $CrV_{1-x}Sb_xO_4$, has been mechanochemically synthesized from the mixture of $Cr_2O_3 \cdot H_2O$, V_2O_5 and Sb_2O_5.

Design and synthesis of four coordination polymers generated from 2,2′-biquinoline-4,4′-dicarboxylate and aromatic bidentate ligands
Junwei Ye, Ping Zhang, Kaiqi Ye, Hongyu Zhang, Shimei Jiang, Ling Ye, Guangdi Yang and Yue Wang
Page 438

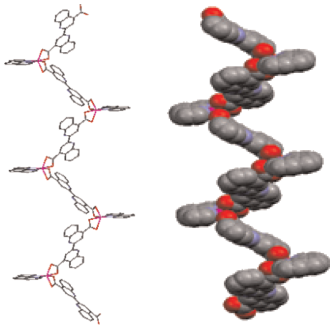

One-dimensional coordination polymer chains.

Synthesis of nanostructured $LiTi_2(PO_4)_3$ powder by a Pechini-type polymerizable complex method
C.R. Mariappan, C. Galven, M.-P. Crosnier-Lopez, F. Le Berre and O. Bohnke
Page 450

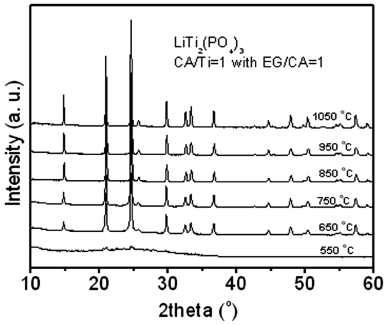

XRD patterns of the powder precursor with CA/Ti = 1 and EG/CA = 1, after heat-treatment at different temperatures for 2 h.

Preparation of uniform rhodamine B-doped SiO_2/TiO_2 composite microspheres
Fuyong Yang, Ying Chu, Lei Huo, Yang Yang, Yang Liu and Jinglin Liu
Page 457

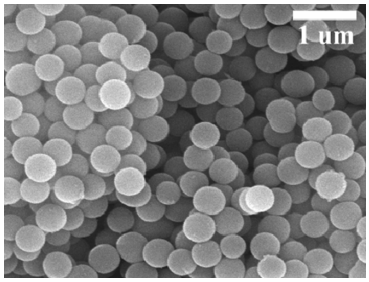

SEM image of RB-doped SiO_2/TiO_2 particles calcined at 800 °C.

Two new titanium molybdenum arsenides: Ti_2MoAs_2 and Ti_3MoAs_3, ternary substitution variants of V_3As_2 and β-V_4As_3
Abdeljalil Assoud, Shahab Derakhshan, Katja M. Kleinke and Holger Kleinke
Page 464

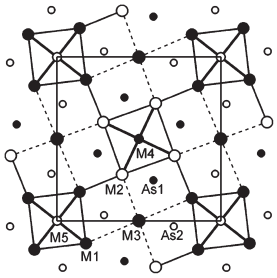

The two title compounds (shown here: Ti_2MoAs_2) simulate vanadium arsenides by Ti/Mo mixtures on the original V sites ($M1$–$M5$).

Polystyrene-ZnO core-shell microspheres and hollow ZnO structures synthesized with the sulfonated polystyrene templates
Yang Yang, Ying Chu, Yanping Zhang, Fuyong Yang and Jinglin Liu
Page 470

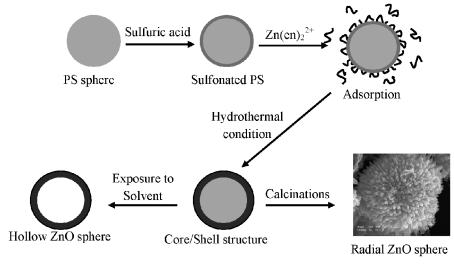

Schematic illustration for the fabrication of PS-ZnO core-shell microspheres and hollow ZnO structures.

The chemical changes occurring upon cycling of a SnO_2 negative electrode for lithium ion cell: In situ Mössbauer investigation

I. Sandu, T. Brousse, D.M. Schleich and M. Danot

Page 476

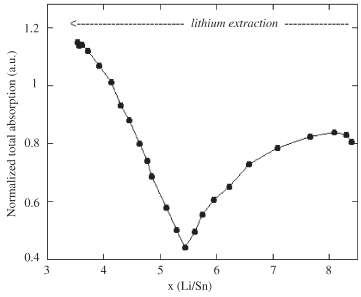

The first oxidation step of a ($Li_{4.4}Sn + 2Li_2O$) electrode could have been expected to consist in progressive lithium extraction from the $Li_{4.4}Sn$ alloy ($x = 8.4$) for β-Sn ($x = 4$) to be formed. The variation of the ^{119}Sn Mössbauer absorption area vs the overall lithium content shows that it is not the case and that a new mechanism takes place when the alloy reaches the composition $Li_{1.4}Sn$ ($x = 5.4$).

Magnetic study of two isotypic manganese chloro-sulfides: $MnSbS_2Cl$ and the new compound $MnBiS_2Cl$

Charlotte Doussier, Gilles André, Philippe Léone, Etienne Janod and Yves Moëlo

Page 486

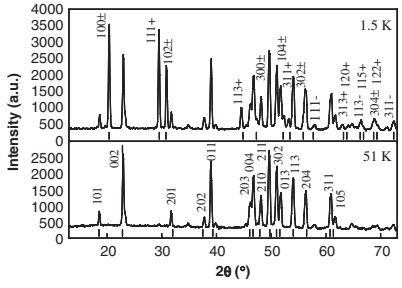

The crystal structure of a new Bi chloro-sulfide was resolved. The two isotypic compounds, $MnSbS_2Cl$ and $MnBiS_2Cl$, were studied for their magnetic properties; magnetic susceptibility and specific heat measurements are presented. Neutron diffraction revealed the incommensurate modulation of the magnetic structure of the Sb compound.

Polycarboxylic acids as network modifiers for water durability improvement of inorganic–organic hybrid tin-silico-phosphate low-melting glasses

Bouzid Menaa, Megumi Mizuno, Masahide Takahashi, Yomei Tokuda and Toshinobu Yoko

Page 492

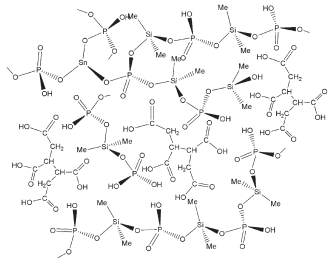

Representation of the possible structure formed with the enhancement of the polycondensation and the chain-like structure formation after addition of acid (butane tetracarboxylic acid is shown as an example in the figure).

Structure and magnetic properties of the orthorhombic $n = 2$ Ruddlesden–Popper phases $Sr_3Co_2O_{5+\delta}$ ($\delta = 0.91$, 0.64 and 0.38)

L. Viciu, H.W. Zandbergen, Q. Xu, Q. Huang, M. Lee and R.J. Cava

Page 500

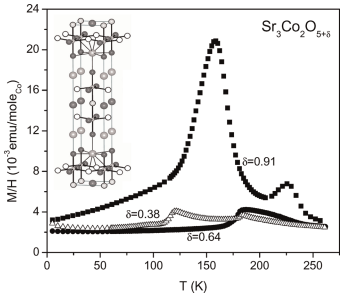

Temperature dependence of the magnetic susceptibility for reduced Ruddlesden–Popper phases, $Sr_3Co_2O_{5+\delta}$ with $\delta = 0.91$, 0.64 and 0.38. The average crystal structure of these phases is shown in inset.

Neutron diffraction and MAS NMR of Cesium Tungstate defect pyrochlores

K.R. Whittle, G.R. Lumpkin and S.E. Ashbrook

Page 512

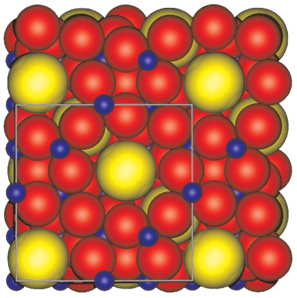

Unit cell representation of $CsTi_{0.5}W_{1.5}O_6$, projection of the [110] plane. Yellow spheres are Cs^+, red spheres are O^{2-} and blue spheres are the *B*-site.

Structural, microstructural and vibrational characterization of apatite-type lanthanum silicates prepared by mechanical milling

E. Rodríguez-Reyna, A.F. Fuentes, M. Maczka, J. Hanuza, K. Boulahya and U. Amador

Page 522

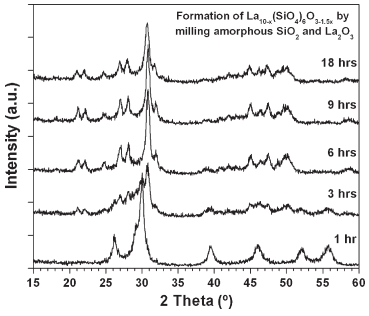

Crystalline apatite-type lanthanum silicates obtained at room temperature by mechanical milling stoichiometric mixtures of elemental oxides in a planetary ball mill.

Continued

Microstructure and luminescence of transparent glass ceramic containing Er^{3+}:BaF_2 nano-crystals
Daqin Chen, Yuansheng Wang, Yunlong Yu, En Ma and Lihua Zhou
Page 532

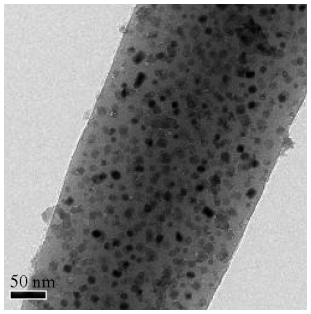

Transparent glass ceramics containing BaF_2 nano-crystals doped with Er^{3+} were prepared by sol–gel route. The upconversion emissions emerged when the sample was heat-treated at 800 °C.

Synthesis and characterization of molybdenum carbides using propane as carbon source
Xiao-Hui Wang, Hong-Ling Hao, Ming-Hui Zhang, Wei Li and Ke-Yi Tao
Page 538

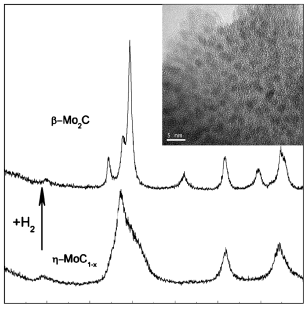

A post-treatment by hydrogen causes the phase transformation of molybdenum carbides in both the conventional TPRe method and a rapid heating method. The HRTEM image shows fairly uniform particles of β-Mo_2C display an excellent dispersion on amorphous SiO_2 support.

Structural behavior of $Sr_2Bi_2O_5$ at high pressures
F.X. Zhang, B. Manoun, S.K. Saxena and C.S. Zha
Page 544

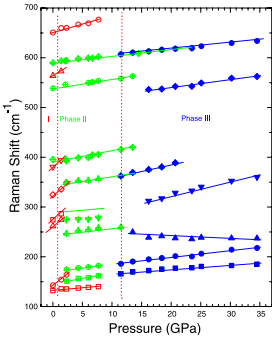

Pressure dependence of the frequency of the observed Raman modes for orthorhombic $Bi_2Sr_2O_5$ clearly indicates the phase transition.

A structure and phase analysis investigation of the "1:1" ordered A_2InNbO_6 perovskites ($A = Ca^{2+}$, Sr^{2+}, Ba^{2+})
V. Ting, Y. Liu, R.L. Withers, L. Norén, M. James and J.D. Fitz Gerald
Page 551

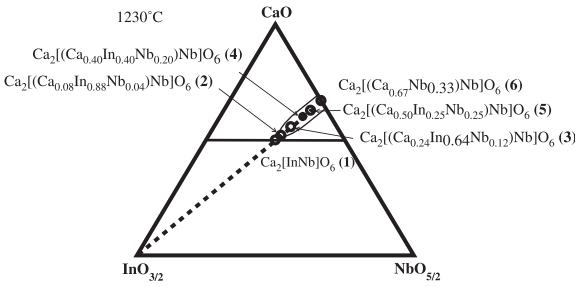

Ternary phase diagram showing the compositions investigated along the quasi-binary join between the $Ca_2[InNb]O_6$ 1:1 material and the $Ca_2[(Ca_{0.6}7Nb_{0.33})Nb]O_6$ perovskite structure.

Synthesis, structure and physical properties of Ru ferrites: $BaMRu_5O_{11}$ (M = Li and Cu) and $BaM'_2Ru_4O_{11}$ (M' = Mn, Fe and Co)
M.L. Foo, Q. Huang, J.W. Lynn, Wei-Li Lee, Tomasz Klimczuk, I.S. Hagemann, N.P. Ong and R.J. Cava
Page 563

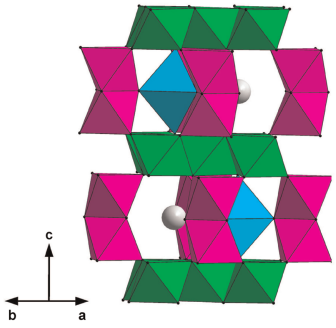

The representative crystal structure of R-type ferrite $BaMRu_5O_{11}$ (M = Li and Cu) and $BaM'_2Ru_4O_{11}$ (M' = Mn, Fe and Co) with emphasis on the transition metal–oxygen polyhedra. Edge sharing octahedra are shaded green; face sharing octahedra are shaded magenta; isolated trigonal bipyramids are shaded cyan; barium atoms are shaded grey.

Metal phosphonates containing pyridyl N-oxide groups: Syntheses of $Cd\{(2\text{-}C_5H_4NO)CH(OH)PO_3\}(H_2O)_2$ and $Zn\{(4\text{-}C_5H_4NO)CH(OH)PO_3\}$ with chain and layer structures
Deng-Ke Cao, Yi-Zhi Li and Li-Min Zheng
Page 573

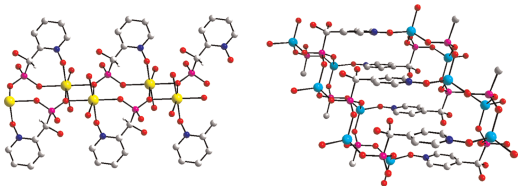

This paper reports the syntheses and characterization of two polymeric phosphonate compounds incorporating pyridyl N-oxide groups namely $Cd\{(2\text{-}C_5H_4NO)CH(OH)PO_3\}(H_2O)_2$ (**1**) with a chain structure and $Zn\{(4\text{-}C_5H_4NO)CH(OH)PO_3\}$ (**2**) with a layer structure.

Synthesis, structural determination and magnetic properties of layered hybrid organic–inorganic, iron (II) propylphosphonate, Fe[$(CH_3(CH_2)_2PO_3)(H_2O)$], and iron (II) octadecylphosphonate, Fe[$(CH_3(CH_2)_{17}PO_3)(H_2O)$]
Carlo Bellitto, Elvira M. Bauer, Philippe Léone, Alain Meerschaut, Catherine Guillot-Deudon and Guido Righini
Page 579

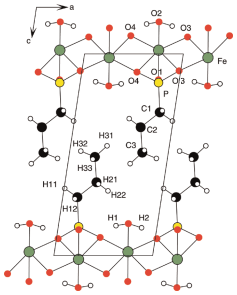

Unit-cell packing of Fe[$(CH_3(CH_2)_2PO_3)(H_2O)$] viewed along the *b*-axis.

Nanosized $LiMn_2O_4$ from mechanically activated solid-state synthesis
V. Massarotti, D. Capsoni and M. Bini
Page 590

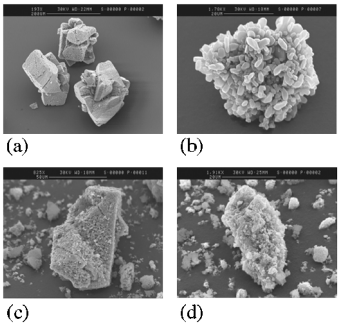

SEM micrographs of (a) MnO, (b) Li_2CO_3, (c) Li_2CO_3/MnO manually grinded stoichiometric mixture and (d) the same mixture after 5 h mechanical grinding.

Structure, energy band, and optical properties of $NaLa(PO_3)_4$ crystal
J. Zhu, W.-D. Cheng, D.-S. Wu, H. Zhang, Y.-J. Gong and H.-N. Tong
Page 597

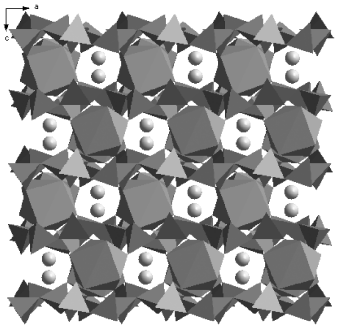

LaO_8 polyhedra and $[(PO_3)_4]^{4-}$ chains share oxygen atoms to form a three-dimensional framework, delimiting intersecting tunnels in which the sodium ions are located.

NOTICE

The Keyword Index for Volume 179 will appear in the December 2006 issue as part of a cumulative index for the year 2006.